OPEN ACCESS
IOP Publishing
Journal of Physics: Condensed Matter
J. Phys.: Condens. Matter **36** (2024) 415805 (11pp)
https://doi.org/10.1088/1361-648X/ad5d3f

Tailoring magnon modes by extending square, kagome, and trigonal spin ice lattices vertically via interlayer coupling of trilayer nanomagnets

Julius de Rojas[1,2,*], **Del Atkinson**[1] and **Adekunle O Adeyeye**[1,*]

[1] Department of Physics, Durham University, Durham DH1 3LE, United Kingdom
[2] Department of Physics, Oklahoma State University, Stillwater, OK 74078, United States of America

E-mail: julius.de_rojas@okstate.edu and adekunle.o.adeyeye@durham.ac.uk

Received 26 March 2024, revised 13 June 2024
Accepted for publication 28 June 2024
Published 18 July 2024

Abstract

In this work high-frequency magnetization dynamics and statics of artificial spin-ice lattices with different geometric nanostructure array configurations are studied where the individual nanostructures are composed of ferromagnetic/non-magnetic/ferromagnetic trilayers with different non-magnetic thicknesses. These thickness variations enable additional control over the magnetic interactions within the spin-ice lattice that directly impacts the resulting magnetization dynamics and the associated magnonic modes. Specifically the geometric arrangements studied are square, kagome and trigonal spin ice configurations, where the individual lithographically patterned nanomagnets (NMs) are trilayers, made up of two magnetic layers of $Ni_{81}Fe_{19}$ of 30 nm and 70 nm thickness respectively, separated by a non-magnetic copper layer of either 2 nm or 40 nm. We show that coupling via the magnetostatic interactions between the ferromagnetic layers of the NMs within square, kagome and trigonal spin-ice lattices offers fine-control over magnetization states and magnetic resonant modes. In particular, the kagome and trigonal lattices allow tuning of an additional mode and the spacing between multiple resonance modes, increasing functionality beyond square lattices. These results demonstrate the ability to move beyond quasi-2D single magnetic layer nanomagnetics via control of the vertical interlayer interactions in spin ice arrays. This additional control enables multi-mode magnonic programmability of the resonance spectra, which has potential for magnetic metamaterials for microwave or information processing applications.

Supplementary material for this article is available online

Keywords: magnonics, mangetization dynamics, artificial spin ice, mangetic nanostructures, metamaterials, nanomagnets, microwave devices

* Authors to whom any correspondence should be addressed.

1. Introduction

Continued manufacturing limitations and the need for increasing energy efficiency are two factors that challenge Moore's Law scaling [1, 2]. Directing research interest towards novel energy efficient devices that can operate in the low to high GHz regime and are inherently low-energy is a key driver for magnonics research. Magnonics is an emerging subfield of spintronics that utilizes quantized spin-waves (the 'magnons') to efficiently propagate and process high frequency signals. Magnonics has the potential to be deployed in energy-efficient devices [3–11] and as a platform for alternative next-generation computing [12–21].

The nanomagnets (NMs) that make up the extended arrays that are suitable for magnonics offers the potential to tune the behavior of the propagating magnons, which depends strongly on the material, size, shape, spacing and arrangement of the NMs through which they propagate [22], a result of changing the shape anisotropy and the demagnetizing and interaction fields. Increasing attention has been paid to periodic arrangements of NMs, known as magnonic crystals (MCs), where the physical arrangement of the NMs can be used to tailor the spin-wave behavior. The interplay between NMs has been explored in 1D lattices of nanowires with modulated magnetic properties or shape [23–26], as well as 2D lattices of dots and antidots [27–33].

Artificial Spin Ice (ASI) lattices have emerged as magnetic metamaterials which possess a high degree of tunability in MC applications [34–37]. ASI lattices are composed of two-dimensional, geometrically frustrated lattices of NMs that leverage the geometrical arrangement and spacing between individual NMs to tune the magnetostatic interactions, which can be used in concert with the magnetocrystalline and shape anisotropy of the individual NMs to control the collective magnetization states and spin-wave behavior [38–49]. Among the ASI structures studied are square, kagome, tetragonal, tetris, pinwheel, and shatki lattices [50–57], as well as plaquettes of coupled NMs [58, 59]. Recently, focus has been directed towards extending MCs beyond the plane to 3D nanostructures [60, 61] which present rich magnetization states and spin-wave behavior not seen in 2D lattices, and has been the subject of recent work on structures such as scaffolds [62], tetrapods [63–65], gyroids [66], and nanovolcanoes [67], among other exciting work [68–73]. However, fabricating complex 3D structures is currently time-consuming and incompatible with industrial fabrication equipment. Accessing the out-of-plane dimension using standard lithography has limitations in 3D NM structure shape, but would enable additional tunability of the magnon spectra, and increase the programmable degrees of freedom in MCs via industrially compatible processes. Such a degree of freedom can be tuned via interlayer-coupling within multilayered nanostructures, where two ferromagnetic layers are separated by a nonmagnetic layer. Changing the thickness of the spacer layer modifies the dipolar coupling between the ferromagnetic layers of a multilayered NM structure, which in turn will tune the magnetization states at a given field and the resonance modes. The magnetization dynamics in lattices composed of trilayer magnets has been studied in nanowires [24, 25] and nanodots [32], but so far the magnetostatic and magnetization dynamics of ASI lattices composed of trilayered NMs has been limited to square spin ice lattices, where dipolar interactions allows for bespoke resonance mode tuning [74] and strong magnon-magnon coupling and a large number of configurable ground states [75]. However, the behavior of trilayer ASI lattices with higher symmetries and a larger number of resonance modes, such as kagome or trigonal lattices, has to date not been systematically reported.

In this work we study the quasi-static and dynamic magnetization behavior of three distinct ASI-type lattices: square spin ice (SSI), kagome spin ice (KSI), and trigonal spin ice (TSI) lattices, wherein each NM is a trilayer stack composed of two $Ni_{81}Fe_{19}$ (Permalloy, Py) layers with thicknesses of 30 nm and 70 nm, separated by a copper spacer layer of varying thickness. The distinct static and dynamic behavior of the individual ferromagnetic layers for each ASI was first assessed. The effect of interlayer coupling was then investigated with two different Cu spacer layer thicknesses ($t_{Cu} = 2$ nm and 40 nm) where quasi-static magnetic hysteresis and dynamic resonance spectra are reported for each geometry. The KSI and TSI lattices introduce an additional tunable resonance mode by symmetry and the trilayer structure enables tunability between all 3 modes by varying t_{Cu}. The spacing between modes also depends strongly on the geometrical arrangement of the trilayer NMs, demonstrating that the interplay of interlayer coupling between the ferromagnetic layers and the ASI NM geometrical arrangement enables further tuning of the magnetic hysteresis and the resulting magnonic spectra in the kagome and trigonal lattices. This is confirmed by micromagnetic simulations of the remanent fields, which highlights that the coupling within the NMs in 2D lattices as a powerful factor for extending control towards true 3D structured ASI lattices for microwave and functional magnonic applications.

2. Method

2.1. Sample fabrication

A set of artificial spin ice (ASI) lattices composed of trilayered Permalloy/Cu were grown on 5 $\times$ 5 $\times$ 0.5 mm^3 silicon (100) substrates. Permalloy ($Ni_{81}Fe_{19}$, Py) and Cu were evaporated using a custom-built ultra-high vacuum thermal evaporator with a base pressure of 1.0×10^{-7} Torr. Films were deposited at a rate of 0.2 Å s^{-1}, monitored by a quartz crystal oscillator that was calibrated via x-ray reflectivity using a Bruker D8 Advance. The ASIs were patterned using deep UV (DUV) photolithography, as discussed in Adeyeye and Singh [76], over a square area of 4 $\times$ 4 mm^2. Evaporation was followed by ultrasonic lift-off with acetone and then isopropyl alcohol. A schematic of the NM structure examined in this work is presented in figure 1(a), for the case of a KSI lattice. Long-range order and uniformity was confirmed in reciprocal space by in-plane x-ray diffraction scattering (figure 1(b)), where the regular satellite peak spacing corresponds to the array periodicity which is consistent with the NM spacing measured along the

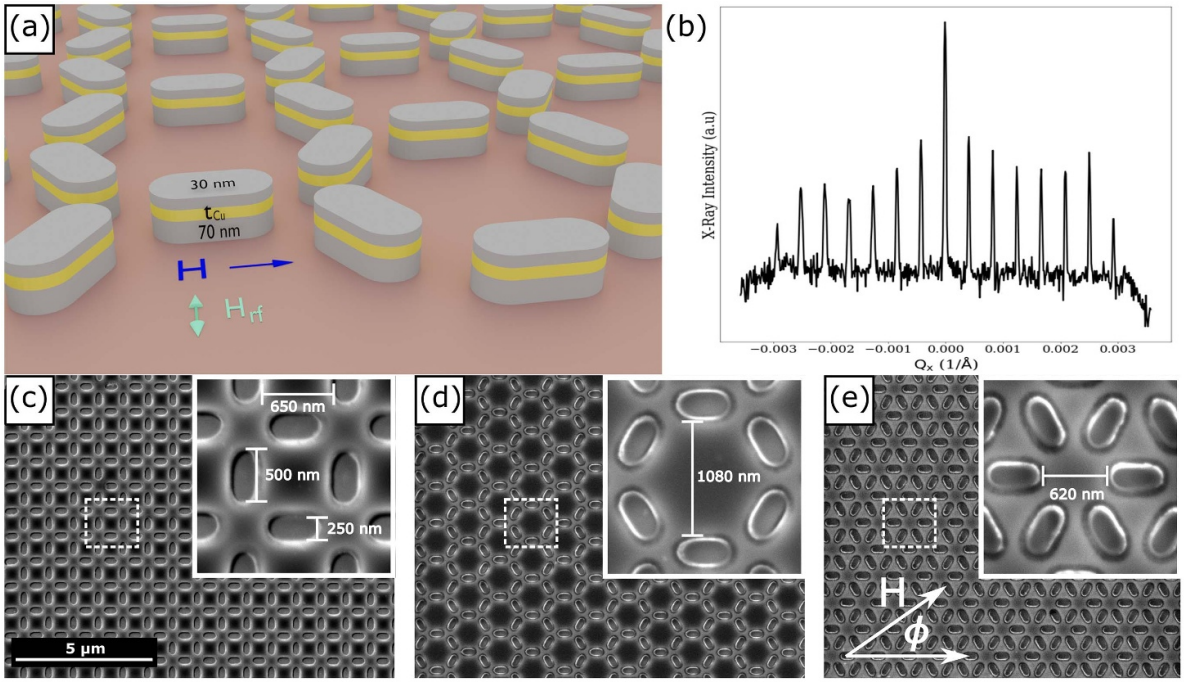

Figure 1. (a) Schematic of a kagome spin ice (KSI) lattice composed of trilayer nanomagnets, with the direction of H and H_{rf} indicated. (b) X-ray diffraction of the sample structure, confirming high degree of periodicity over the entire patterned substrate area. (c)–(e) SEM images of the square, kagome, and trigonal lattices, respectively. Insets shows magnified image corresponding to dotted white boxes, along with nanomagnet dimensions and relevant lattice spacing. (e) Direction H, ϕ, is measured relative to the horizontal axis of each lattice shown.

diagonal of the square spin ice lattice, $\phi = 45°$. Representative scanning electron microscopy (SEM) images of the ASI lattices studies are shown in figures 1(c)–(e) for SSI, KSI, and TSI arrangements. This structural analysis confirm good lift-off and uniformity of the NMs over large areas. The individual NM in the ASIs are the same with a width of 250 nm and a length of 500 nm. For the SSI lattices, the edge-to-edge spacing is 650 nm (figure 1(c), inset). For the KSI lattices, the edge-to-edge spacing between elements opposite the kagome structure is 1080 nm (figure 1(d), inset), while in TSI lattices neighboring, parallel NMs are spaced by 620 nm along their long axis (figure 1(e), inset). Within these three ASI structures, the layering of the individual NMs were tuned. Each NM is a trilayer of Py[70 nm]/Cu[t_{Cu}]/Py[30 nm], with $t_{Cu} = 2$ or 40 nm.

2.2. Experimental characterization

A Lake Shore vibrating sample magnetometer (VSM) was used to measure magnetization as a function of applied field to generate magnetic hysteresis (M-H) loops at room temperature. Measurements were performed with the field applied in-plane and oriented along either $\phi = 0°$ or 45° relative to the ASI patterns, see figure 1(e). M-H loops were measured over a field range of ±5 kOe. M was defined as the total magnetic moment of each sample and the saturation magnetization (M_S) was M measured at +5 kOe, after correcting for a linear background. Alongside the M-H loops, a normalized susceptibility, $(\mathrm{d}M/\mathrm{d}H)/M_S$, was determined for one-half of the magnetization curve (from positive to negative saturation) from a weighted linear least squares regression with a window of 5 neighboring points.

Dynamic magnetic behavior was measured by ferromagnetic resonance (FMR) spectroscopy using a fixed-frequency field-sweep mode. The ASI arrays were placed onto a coplanar waveguide in flip-chip configuration (face down). A fixed, in-plane RF field, H_{rf}, between 8–16 GHz was then generated by a Rohde & Schwarz Vector Network Analyzer and propagated through the coplanar waveguide, at frequency steps of $\leqslant$ 0.5 GHz. H_{rf} is oriented in-plane and orthogonal to an applied external field, H (figure 1(a)). H was swept from +5 kOe to 0 Oe using a field modulation technique, with a broadband microwave detector diode coupled to a lock-in amplifier. The derivative of the absorbed power with respect to the applied field ($\mathrm{d}P/\mathrm{d}H$) was then measured for each frequency.

2.3. Micromagnetic simulations

Micromagnetic simulations were performed using the GPU-accelerated software mumax^3 [77]. The Py parameters used include a saturation magnetization of $M_S = 800$ emu cc^{-1}, a magnetocrystalline anisotropy constant of $K = 0$, an exchange constant of $A = 1.3 \times 10^{-6}$ erg cm^{-1}, and a damping parameter of $\alpha = 8.0 \times 10^{-3}$ [78]. Individual NM dimensions and lattice spacing were obtained from SEM images, and were masked onto on atlases of 1.8 $\times$ 1.8 μm^2 (SSI), 2.3 $\times$ 1.33 μm^2 (KSI), and 1.12 $\times$ 1.94 μm^2 (TSI) in area. All simulations use cubic cells of 5 $\times$ 5 $\times$ 5 nm^3 in volume, with

2D periodic conditions. M-H loops were simulated using 2 mT steps from a saturation field of 500 mT, with the B field applied along the x-direction and minimizing stop value of $dm = 1 \times 10^{-6}$. Simulated FMR frequency sweeps and spatial resonance modes were done using a sinc pulse of 20 GHz with an amplitude of 0.5 mT. Time evolution was limited to 4 ns as the signal was damped to nearly zero beyond this value. Time steps were chosen to be 10 ps, well below the Nyquist Sampling Theorem condition. FMR simulations were computed using a Fast Fourier Transform (FFT), with an added Hanning window to reduce leakage during FFT processing.

3. Results and discussion

As a starting point to understand the emergent behavior resulting from the ferromagnetic/non-magnetic/ferromagnetic (FM/N/FM) trilayered NMs, the static and dynamic magnetization behavior of each of the ferromagnetic sublayers comprising the trilayer NMs is first presented for each ASI array geometry. Magnetization vs field (M-H) hysteresis loops are presented in figure 2 for a single layer of the three ASI lattices studied, one for each of the Py layers comprising the trilayer stack, with H directed along $\phi = 0°$ for each measurement. For ease of comparison, data previously reported for the SSI case [74] is plotted alongside the M-H loops for TSI and KSI lattices. The M-H loops are plotted along with the normalized susceptibility, $(\mathrm{d}M/\mathrm{d}H)/M_S$ (dashed lines), which is provided to highlight significant features during the magnetization reversal such as, for example, nucleation and annihilation of the vortices. The susceptibility is shown for features which occur as the M-H is swept from positive to negative saturation. ASIs composed of 30 nm thick single-layer NMs (figures 2(a)–(c)), black) all show three clear steps. An initial NM macrospin state is followed by the nucleation and annihilation of vortices within the NMs where the easy axes are aligned either parallel ($\phi = 0°$), along the hard axis perpendicular ($\phi = 90°$) or tilted by 60°, to the applied field. The effect of the KSI and TSI array geometries are observed in the field values at which these features occur. In the SSI case (figure 2(a)), the features appear ~0, 500, and −1300 Oe, while in the KSI case (figure 2(b)) the features are comparable in scale and field. The KSI features are also shared with the TSI samples (figure 2(c)), and can be understood as the result of the orientation of the NMs whose hard axis is 60° away from the field direction, resulting in reversal at lower field. For the 70 nm thick NM ASI lattices (figures 2(a)–(c)), red), again the behavior is similar, but not all of the features are shared across the ASIs. The M-H loop for the 70 nm-thick Py SSI shows five distinct reversal features, consistent with the nucleation and annihilation of two vortices in each NM and initial features at ~2 kOe, as reported earlier [74]. Indeed, nucleation and annihilation fields near ± 500 Oe are observed in all cases. However, while the 70 nm KSI sample also shows 5 reversal features, features near 2 kOe are suppressed due to a much larger spread in nucleation and annihilation at high field, spanning 1.2–2 kOe. These features are similar in the TSI case. The largest difference between KSI and TSI occurs around zero field.

First, the dynamic magnetic behavior of each of the single layer ASIs was measured by ferromagnetic resonance (FMR) spectroscopy. If we consider each NM in the ASI latices individually, then the measured resonance spectra can be modeled by the Kittel equation [79]. For a given applied field H (taken to be in the x-y plane), the resonance frequency is given by $f_{\mathrm{Res}} = \gamma/2\pi\sqrt{\left(H + \left(N_z - N_{\|}\right)4\pi M_S\right)\left(H + \left(N_{\perp} - N_{\|}\right)4\pi M_S\right)}$, where γ is the gyromagnetic ratio, $4\pi M_S$ is the magnetization of the sample, $N_{\|}$ and $N_{\perp}$ are the demagnetization factors that are parallel and perpendicular to the applied field, respectively, and N_z is the demagnetization factor in the z direction (along the NM thickness). More significantly, figures 2(d)–(f) shows the FMR spectra measured at 12 GHz for the SSI, KSI and TSI lattices, respectively. In all cases, two distinct resonance fields H_{R1} and H_{R2} are observed as a function of the field applied along $\phi = 0°$. This can be explained by the demagnetization factors of the NMs and ASI geometry. If the NMs are assumed to take an approximate ellipsoid shape [80], then the demagnetization factors along the principal axes of the single layer NMs can be compared for the dimensions of the NMs in this work. For the SSI case, there are only two orientations of the NMs relative to $\phi = 0°$: NMs whose easy axis are aligned with the field ($N_{\perp} > N_{\|}$), and NMs whose easy axis are perpendicular to the applied field ($N_{\|} > N_{\perp}$). We may then attribute the resonance mode at lower fields, H_{R1}, to the resonance modes localized in NMs whose easy axis are parallel to H, and the modes at higher fields, H_{R2}, with modes localized in NMs whose easy axis is perpendicular to the applied field. The KSI and TSI lattices also have two possible NM orientations relative to the applied field, with NM easy axes either parallel or tilted 60° away from the applied field, with corresponding resonance fields H_{R1} and H_{R2}. Comparing across 30 nm and 70 nm thicknesses, we see in each ASI (figures 2(d)–(f)) the resonance modes are shifted, with H_{R2} shifting 0.8–1.2 kOe higher, a result of an increase in the in-plane demagnetization factors ($N_{\|}$ and $N_{\perp}$) and a decrease in N_z, due to a substantial increase in the thickness while the width and length remain fixed.

To understand the effect of increased thickness and to set a baseline for comparing with the multilayered NMs, the micromagnetic software mumax[3] was used to model the remanent field emerging along the center of the ASIs. Figures 2(g)–(i) shows vector field plots of the remanent field, H_d, in the x-y plane at the midpoint thickness of the 70 nm layer. Simulations of ASIs with thicknesses of 30 nm have been reported elsewhere [50, 74]. The remanent fields in each of the 70 nm-thick ASIs are in a mixture of closed-loop states including bi-vortices of opposite chirality and a single vortex. In the SSI case (figure 2(g)), the bi-vortex state is observed along the easy-axis NMs, while the single vortex states lies within the hard axis NMs. This is reversed in the KSI and TSI lattices, where the single vortex states lie within the NMs aligned along the easy axes. It is also worth noting that the

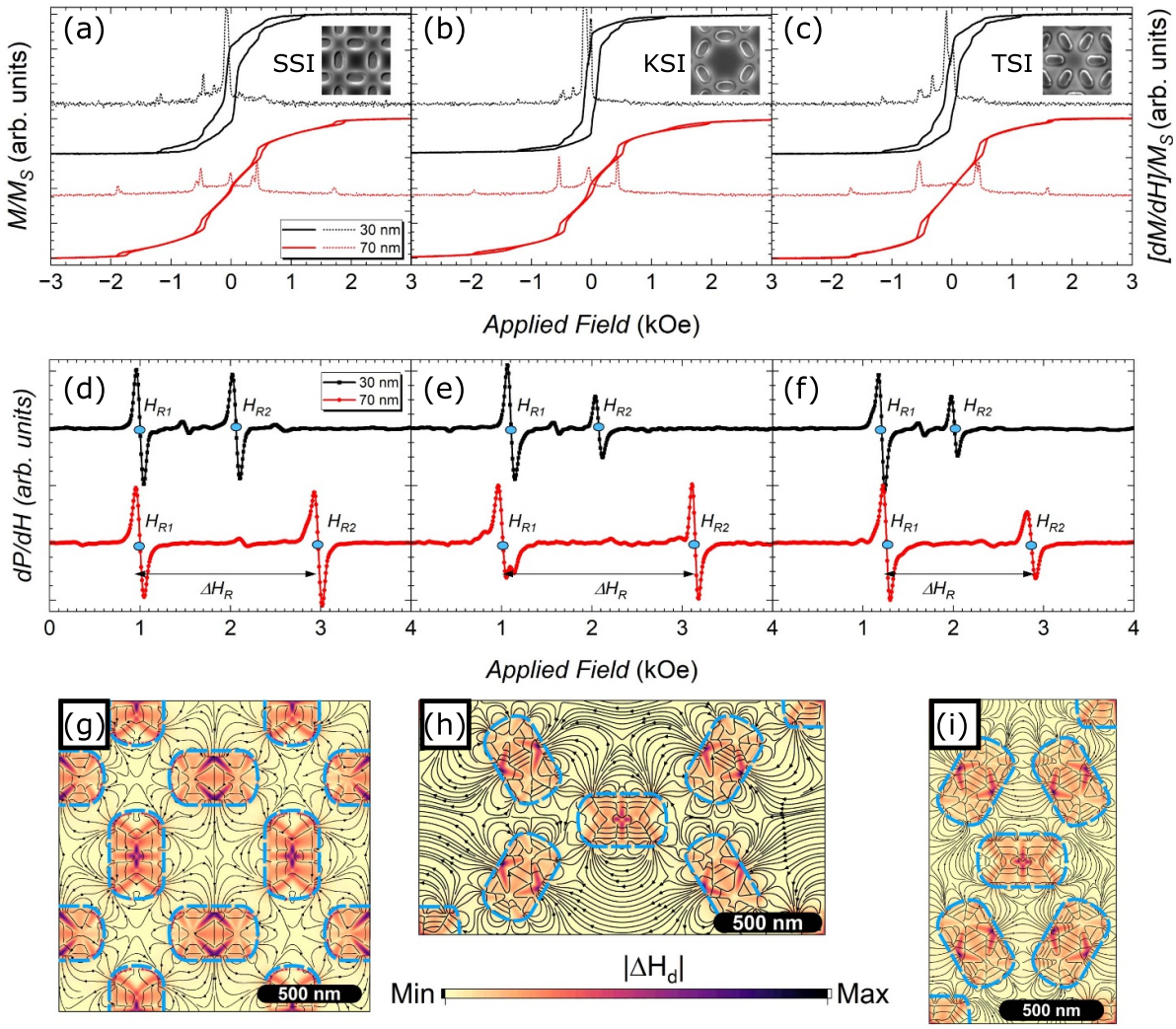

Figure 2. Normalized M-H loops, M/M_S, and susceptibility, $(\mathrm{d}M/\mathrm{d}H)/M_S$, for single layer Py ASIs of 30 nm and 70 nm thicknesses. (a) SSI lattice, (b) KSI lattice and (c) TSI lattice. (d)–(f) show the FMR spectra at 12 GHz for the same NM thicknesses and lattice geometries. The red and black curves correspond to single layer thicknesses of 30 nm and 70 nm, respectively. Measurements were done with an applied field oriented at 0°. Insets (a)–(c) show the geometry of each corresponding ASI. The blue dots in (d)–(f) demarcate resonance fields H_{R1} and H_{R2}. (g)–(i) Simulated remanent fields at the midpoint of each 70 nm-thick Py SSI, KSI, and TSI, respectively.

more complex magnetization states simulated in the 70 nm thick layer may also impact the FMR modes at a given field. Micromagnetically simulated M-H loops for the 30 nm and 70 nm thin NM ASIs are presented in supplementary material.

FM/N/FM trilayers combining 30 nm and 70 nm-thick FM layers were fabricated for each ASI with two distinct N layer thicknesses of 2 and 40 nm of Cu to create the following structures: Py(70 nm)/Cu($t_{\mathrm{Cu}} = 2, 40$ nm)/Py(30 nm). Figures 3(a)–(c) show the M-H loops for trilayered lattices where $t_{\mathrm{Cu}} =$ 2 nm (black) and 40 nm (red) for SSI, KSI, and TSI arrays, respectively (the specific cases of $t_{\mathrm{Cu}} = 2$ nm and 40 nm in SSI previously reported [74] are plotted here for comparison). Two observations are immediately noted. First, for all geometries the nucleation and annihilation for the $t_{\mathrm{Cu}} = 2$ nm case are found to have a wide spread, in contrast to the single layer 70 nm case. This is notably different for the $t_{\mathrm{Cu}} = 40$ nm that reflecting the change in the dipolar coupling between the ferromagnetic layers. Secondly, regardless of the lattice geometry or Cu spacer thickness, the hysteresis has an open loop and a corresponding sharp reversal feature around $H = 0$, which may be attributed to the 30 nm-thick top layer of the trilayer stack (see figure 2(a)). Considering the SSI lattice first, figure 3(a), the nucleation and annihilation reversal behavior seen for $t_{\mathrm{Cu}} = 2$ nm (black) changes in shape and field values when $t_{\mathrm{Cu}} = 40$ nm (red), with reversal features similar to the features of the 70 nm single layer ASI near 500 Oe and 2 kOe. In the KSI case (figure 3(b)), the hysteresis becomes smoother and the open loop extends over a wide field range for the NMs with $t_{\mathrm{Cu}} = 2$ nm spacer, with only very small features highlighted during the M-H loop. For NMs with a $t_{\mathrm{Cu}} = 40$ nm spacer layer, the features associated with the single 70 nm thick FM layer KSI sample are also present around 500 Oe, along with a large feature near 0 Oe that can be associated with the 30 nm layer at the top of the trilayer stack. A similar

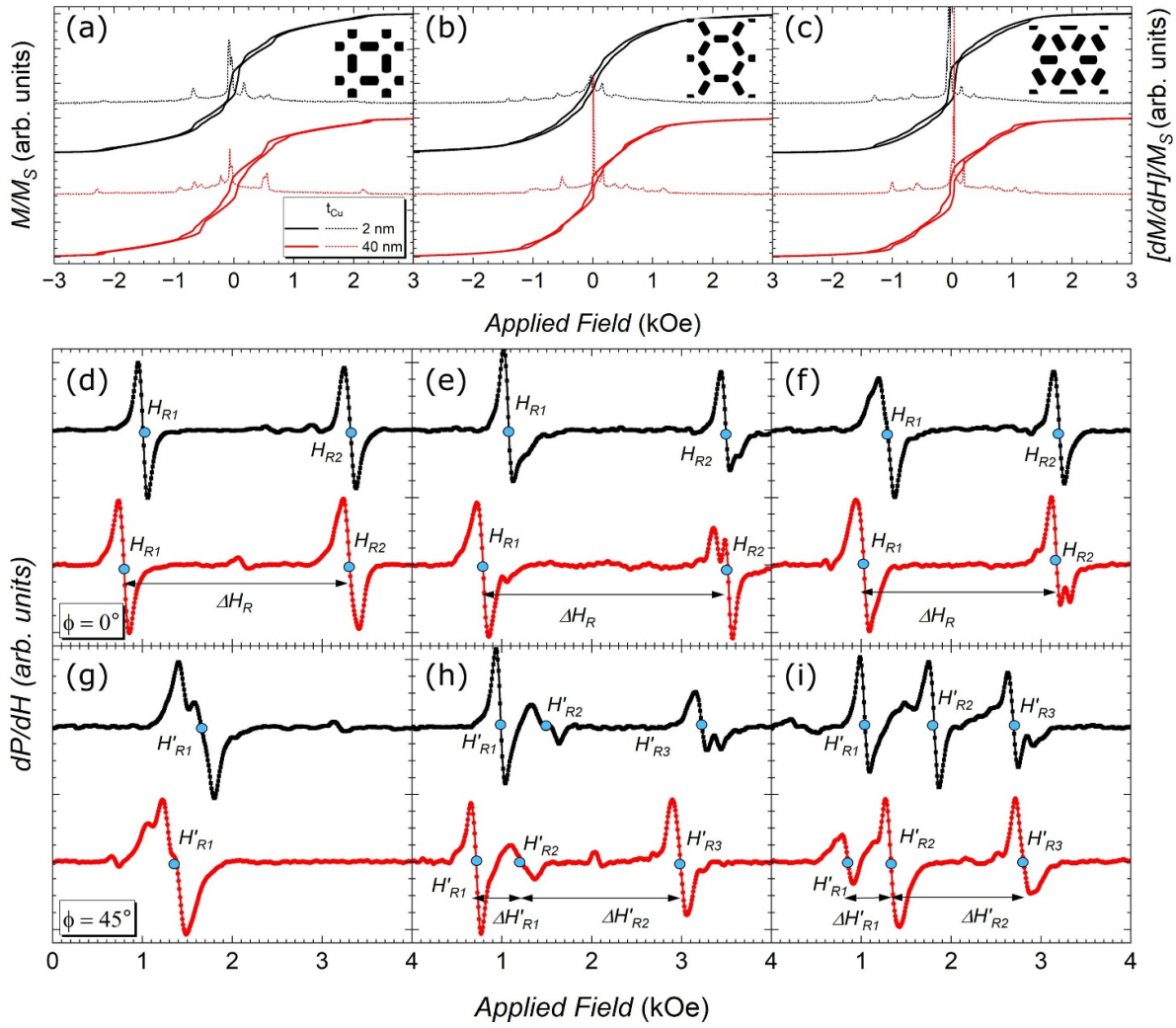

Figure 3. (a)–(c) Normalized M-H loops, M/M_S, and susceptibility, $(\mathrm{d}M/\mathrm{d}H)/M_S$, and (d)–(f) FMR spectra at 12 GHz for trilayer SSI, KSI, and TSI lattices with $t_{\mathrm{Cu}} = 2$ nm (black) and 40 nm (red). The applied field is oriented at $\phi = 0^{\circ}$. ΔH_R notes the spacing between resonance modes H_{R1} and H_{R1}. (g)–(i) FMR spectra at 12 GHz with the applied field oriented at $\phi = 45^{\circ}$, with three resonance modes appearing in KSI and TSI lattices. $\Delta H'_{R1}$ indicates the spacing between H'_{R1} and H'_{R2}, and $\Delta H'_{R2}$ the spacing between H'_{R2} and H'_{R3}. Blue circles indicate locations of resonance modes.

change is observed in the TSI case (figure 3(c)), with an open hysteretic region at higher fields for $t_{\mathrm{Cu}} = 2$ nm that is modified by a sharp feature appearing near 0 Oe, consistent with the 30 nm layer, as well as new features not present in either the 30 nm, 70 nm, or $t_{\mathrm{Cu}} = 2$ case near 1 kOe. The apparent modification of the vortex nucleation/annihilation fields can be attributed to the interlayer coupling between the two Py layers, controlled by the copper spacer thickness, where at large separation the two layers are quasi-independent of each other, while for 2 nm Cu the layers become more strongly magnetostatically coupled, ultimately approaching a single layer.

The modification of the complex magnetization states related to (bi-) vortex nucleation, propagation, and annihilation at each field suggests that the t_{Cu} may also influence the magnetization dynamics of the ASIs. As was the case in figure 2 for $\phi = 0^{\circ}$, two resonance modes appear for each ASI lattice. Figures 3(d)–(f) shows representative FMR spectra measured with the applied field along $\phi = 0^{\circ}$ at a frequency of 12.0 GHz. For the SSI lattice the interlayer coupling causes the two resonance modes H_{R1} and H_{R2} to shift and broaden, with $t_{\mathrm{Cu}} = 40$ nm reducing H_{R1} to ~800 Oe and H_{R2} to 3.3 kOe. Considering the KSI lattice (figure 3(e)), it is observed that the resonance field H_{R1} is also reduced when $t_{\mathrm{Cu}} = 2$ nm is increased $t_{\mathrm{Cu}} = 40$ nm, while H_{R2} is slightly increased. In the TSI case (figure 4(f), H_{R1} is once again reduced by the thicker $t_{\mathrm{Cu}} = 40$ nm spacer layer, while H_{R2} is reduced by 100 Oe.

However, a dynamic additional degree of freedom and potential programmability appears when the applied field is directed along $\phi = 45^{\circ}$. In the SSI case the easy axes of the NMs are all tilted by 45° with respect to the applied field, so the demagnetizing factors are equivalent ($N_{\parallel} = N_{\perp}$), resulting in a single resonance frequency at any given field, H'_R. The effect of increasing the spacer layer thickness t_{Cu} from 2 to 40 nm in SSI (figure 3(g)) is shown here, and was explored in

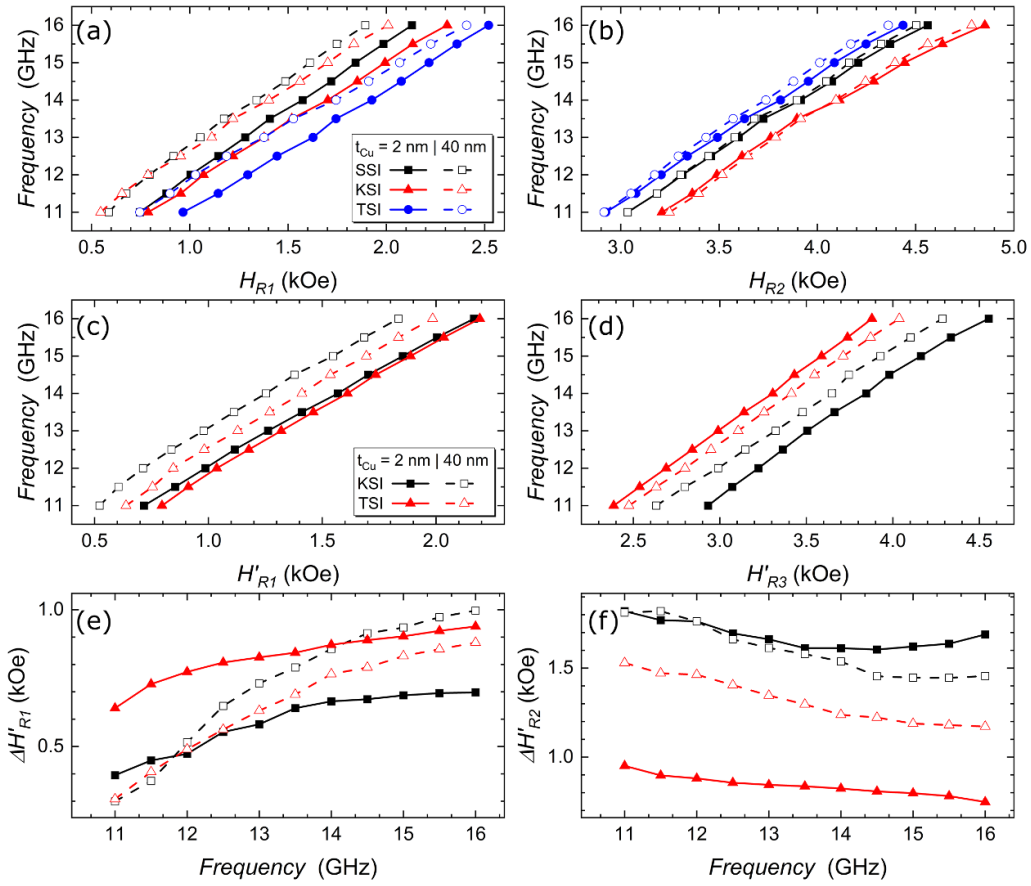

Figure 4. (a)–(b) Frequency as a function of resonance fields for H_{R1} and H_{R2} for different ASI geometries and two Cu spacer layer thicknesses. Kittel curves are shown for SSI, KSI, and TSI measured along $\phi = 0°$ for trilayers with $t_{Cu} = 2$ nm (solid) and $t_{Cu} = 40$ nm (dashed). (c)–(d) Frequency vs. resonance fields H'_{R1} and H'_{R3} for KSI (black) and TSI (red) lattices, when measured along $\phi = 45°$. (e)–(f) Evolution of $\Delta H'_{R1}$ and $\Delta H'_{R2}$ with frequency and copper spacer layer thickness, for KSI and TSI lattice.

depth in a previous work [74]. In contrast, the symmetry of the KSI and TSI lattices results in 3 distinct resonance modes H'_{R1}, H'_{R2}, and H'_{R3}. This is due to three distinct NM orientations relative to the applied field, corresponding to three distinct sets of $N_{\parallel}$ and $N_{\perp}$: easy axes that are tilted 15°, 45°, and 75° away from the applied field. This additional mode offers additional tuning capacity between multiple modes when compared with the SSI lattice. We define $\Delta H'_{R1}$ to be the difference between H'_{R1} and H'_{R2}, and $\Delta H'_{R2}$ to be the difference between H'_{R2} and H'_{R3}. In the KSI case (figure 3(h)), the increase in copper thickness results in a frequency down shift in all resonance modes, with $\Delta H'_{R1}$ and $\Delta H'_{R2}$ increasing. However, in the TSI case, H'_{R1} and H'_{R2} both decrease, but H'_{R3} increases leading to $\Delta H'_{R1}$ decreasing and $\Delta H'_{R2}$ increasing. Taken together these results demonstrate that the combination ASI lattice arrangement and the NM trilayer spacing enables tunable control of the magnon mode frequencies and their relative spacing between each other.

Figures 4(a) and (b) shows how the resonance modes H_{R1} and H_{R2} evolve with frequency for SSI (black), KSI (red), and TSI (blue) lattices with the field aligned along $\phi = 0°$. As the thickness of the copper spacer layer is increased from $t_{Cu} =$ 2 nm to 40 nm the resonance mode H_{R1} shifts downwards for all ASI lattices, in the range 180–230 Oe, and H_{R2} undergoes smaller changes, ~50 Oe, leading to an overall reduction in the ΔH_R for all samples with $t_{Cu} = 40$ nm (see supplementary material for a plot of ΔH_R vs. frequency for samples measured along $\phi = 0°$). However, the effect of increasing thickness has a more complex effect in the KSI and TSI lattices. Figures 4(c) and (d) shows the evolution of resonance modes H'_{R1} and H'_{R3} with frequency for KSI (black), and TSI (red) lattices, where the field is along $\phi = 45°$. Interestingly, H'_{R1} shifts to lower values in both the KSI and TSI case, but not so with H'_{R3}; here, TSI decreases in field value, but KSI increases. With the introduction of the third mode (not plotted here, see supplementary material for H'_{R2}), there can be multiple modes tuned differently depending on the application. If we consider figure 4(e), we see that $\Delta H'_{R1}$ decreases for the TSI lattices, while it increases for KSI lattices. This trend is reversed for the $\Delta H'_{R2}$, where it increases in the TSI case and decreases in the KSI case. Interestingly, there is a clear crossover for $\Delta H'_{R1}$ in the KSI lattice just below 12 GHz. This crossover also occurs in the $\Delta H'_{R2}$ plot (figure 4(f)), corresponding to 12 GHz. Large tunability of spectral spacing of modes, which may potentially increase or decrease with the applied field and the frequencies of choice, is potentially accessible by correctly choosing lattice and interlayer spacing to finely tune multi-mode separation frequencies.

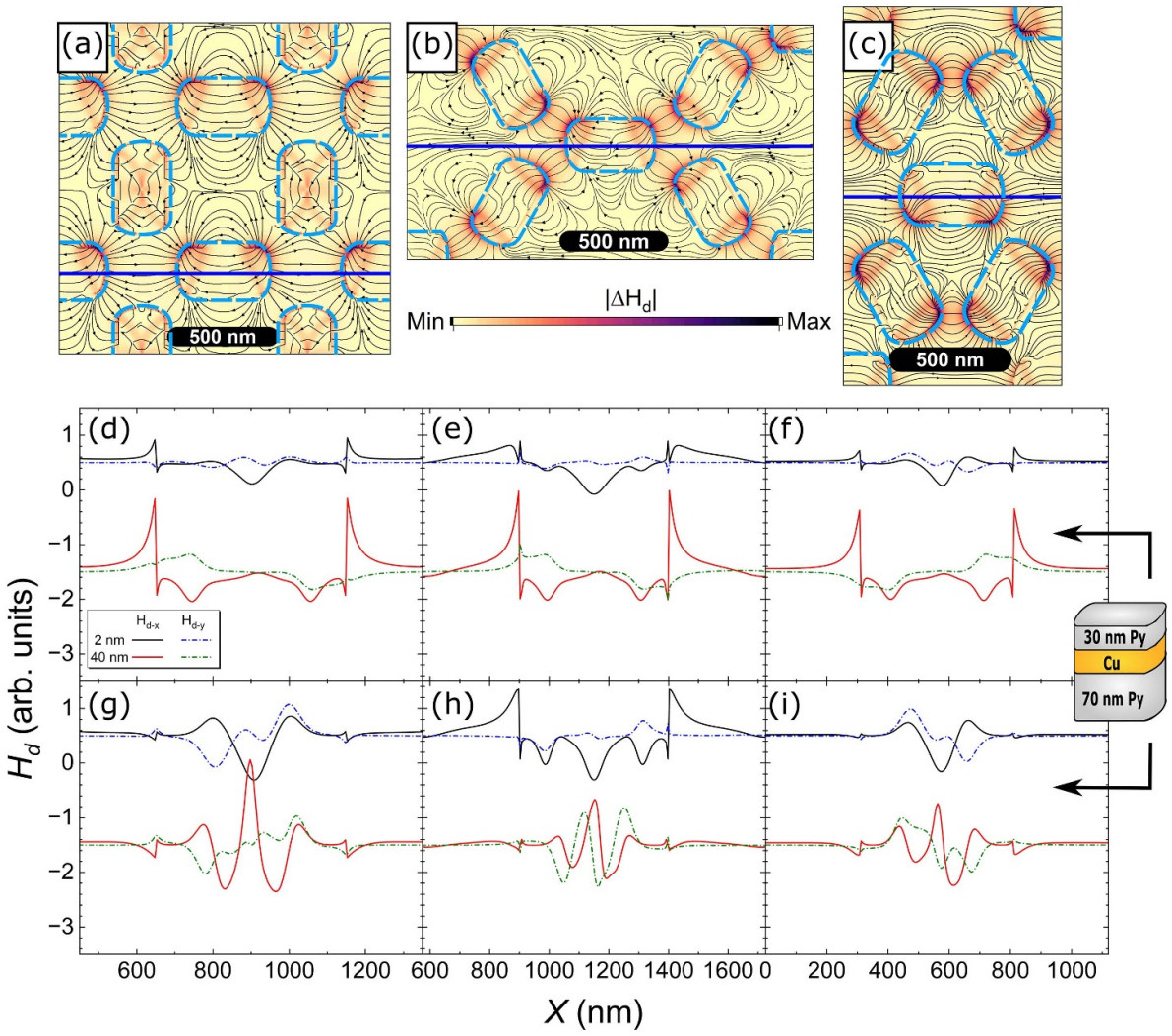

Figure 5. Simulated remanent field, H_d, at the center of each ferromagnetic layer comprising the trilayer stack for SSI, KSI, and TSI lattices (left, center, and right figures, respectively). (a)–(c) Representative plots of the H_d at the midpoint of the 30 nm layer when $t_{\mathrm{Cu}} = 40$ nm. Blue horizontal lines indicate slices along the x-axis for subsequent plots. (d)–(i) x- and y-components of H_d (H_{d-x}, H_{d-y}) in each ferromagnetic layer along the x-direction (blue line), for $t_{\mathrm{Cu}} = 2$ nm and 40 nm. Top row corresponds to the 30 nm layer, bottom row the 70 nm layer. $H_{d-x,y}$ plots for $t_{\mathrm{Cu}} = 40$ nm are offset by 1.5 kOe to allow for easier visualization.

To elucidate how the different ASIs' magnetization states and resonance modes change with increased t_{Cu}, micromagnetic simulations were performed for each stacked ASI (figure 5). The simulations were saturated at 5 kOe along $\phi = 0°$ (x-axis), and then brought back to zero to set the remanent states. As a representative plot, figures 5(a)–(c) shows vector fields plots of the remanent field, H_d, at the midpoint of 30 nm layer atop the trilayer stack for $t_{\mathrm{Cu}} = 5$ nm 40 nm for SSI, KSI, and TSI lattices, respectively. Note that $t_{\mathrm{Cu}} = 5$ nm was chosen for the simulations as $t_{\mathrm{Cu}} = 2$ nm would result in very long computation times due to the large atlas area and relatively tall NMs studied in this work. For the SSI case (figure 5(a)), the remanent state is found to be near the macrospin magnetization state in the NMs whose easy axis is aligned with the applied field, and a single vortex state in NMs aligned along their hard axis. For the KSI and TSI states (figures 5(b) and (c)), it is observed that the remanent state of the 30 nm layer are near-macrospins which conform to spin-ice rules in the ground state, as observed with 2 in(out) and 1 out(in) at each vertex in the KSI lattice. The macrospin states are consistent with the reduced coupling between the layers in the $t_{\mathrm{Cu}} = 40$ nm case.

To further understand how the magnetostatic coupling evolves with increasing Cu thickness in each ASI, line cuts were extracted along the x-axis through the center of each horizontal NM, noted with a blue line. From these line cuts the x and y components of the remanent field, H_{d-x} and H_{d-y} were extracted and plotted in figures 5(d)–(i), with the top (bottom) row corresponding to the 30 (70) nm layer. For clarity and ease of comparison, the $H_{d-x,y}$ plots for $t_{\mathrm{Cu}} = 40$ nm are offset by 1.5 kOe from the $t_{\mathrm{Cu}} = 2$ nm samples. Considering figures 5(d) and (g), the maximum variation in H_{d-x} (ΔH_{d-x}) and H_{d-y} (ΔH_{d-y}) can be assessed in both ferromagnetic layers as the Cu spacer layer thickness is increased from 2 nm to

40 nm for the SSI lattice. As a simple model, the two samples may be treated as effectively a single layer for $t_{Cu} = 2$ nm and two nearly decoupled magnetic layers for $t_{Cu} = 40$ nm. In the $t_{Cu} = 2$ nm case, it is observed in both ferromagnetic layers that ΔH_{d-x} and ΔH_{d-y} are comparable, and so there are competing demagnetization factors due to shape anisotropy and the magnetostatic coupling between NMs and between layers. When $t_{Cu} = 40$ nm, ΔH_{d-x} in both the 30 nm and 70 nm layers (figures 5(d) and (g)) increases relative to ΔH_{d-y}, indicating the demagnetization factor has increased along the x-direction. This corresponds to an increase of the in-plane demagnetizing factors $N_{\parallel}$ and $N_{\perp}$ for each layer and a decrease in N_z relative to the $t_{Cu} = 2$ nm case. While difficult to interpret as easily as a single layer ellipsoid, it can be noted that the sharp increase of the in-plane demagnetizing factor $N_{\parallel}$ and the decrease along N_z for the NMs aligned with the field will result in a modified magnetization state and a shift of H_{R1} to a lower field (figure 4). For the KSI case (figures 5(e) and (h)), ΔH_{d-x} and ΔH_{d-y} are comparable in the 30 nm layer when $t_{Cu} = 2$ nm, and then ΔH_{d-x} once again dominates when $t_{Cu} = 40$ nm, so that the y-axis is again the easy axis, much like the SSI case. However, in the the 70 nm layer (figure 5(h)), ΔH_{d-x} is larger than ΔH_{d-y} when $t_{Cu} = 2$ nm and, following an increase to $t_{Cu} = 40$ nm ΔH_{d-x} and ΔH_{d-y} approach each other, moving from a easy y-axis ($N_{\perp} < N_{\parallel}$) to a state where no axis is clearly easy ($N_{\perp} \approx N_{\parallel}$). This may play a role in the observation that resonance mode spacing is sensitive near 12 GHz, where mode spacing $\Delta H'_{R1}$ and $\Delta H'_{R2}$ can toggle between increasing and decreasing. Indeed, unlike $\Delta H'_{R1}$ for the TSI array and ΔH_R for all arrays, $\Delta H'_{R1}$ for the KSI array crosses near 12 GHz, demonstrating that particular configurations are highly flexible through the frequency range under consideration. In the the TSI case, like the SSI and KSI lattices, finds the 30 nm layer with a easy y-axis, albeit with reduced ΔH_{d-x} when compared to SSI and KSI. Indeed, in the 70 nm case ΔH_{d-x} and ΔH_{d-x} are found to remain near each other in magnitude after increasing t_{Cu} from 2 nm to 40 nm. This complex interplay between shape anisotropy, magnetostatic coupling within NMs and between the NMs within a geometric lattice enables finely-controlled, frequency-dependent multi-mode magnonic tunability.

Moving towards a configurable device with propagating spin-waves would require further work. One potential approach would be to fabricate the ASI structures atop a continuous thin film through which the spin-wave propagates, with the ASIs used to control spin wave propagation [49]. Precise reconfigurability would also be desirable. NM arrays have been demonstrated as spin-wave wave guides in straight and curved geometries [81], where toggling individual NM states can be used to reconfigure the system and control spin wave propagation. In the case of trilayer ASI, recent work by Dion *et al* demonstrated [75] a method to preferentially select the specific macrospin and vortex states in each layer by offsetting each layer in the stack. Exploring asymmetries in KSI or TSI lattices with tri-(or higher) layer NMs can allow for selectively configuring NMs in a host of grounds states, greatly expanding the functionality of the ASI.

4. Conclusion

The static and dynamic magnetization behavior of FM/N/FM trilayered NM structures forming arrays of square, kagome, and trigonal artificial spin ice lattices has been detailed. Each trilayer NM was composed of two ferromagnetic layers with different thicknesses separated by a nonmagnetic copper spacer layer. Multi-mode tunability of the dynamic magnetic resonant properties for a given lattice was observed as a function of the interlayer coupling between the ferromagnetic layers in the constituent NMs. In contrast to the trilayer square lattice, where only one or two modes can be tuned via the copper spacer layer thickness, it was demonstrated here that the interlayer coupling between ferromagnetic layers in kagome and trigonal NM lattices can be used to tune two or three different resonance modes and, in particular, control the relative field spacing between the resonance modes at varying frequencies. This increases the functionality of the MC. This work shows that 'pseudo-3D' multilayering within the individual NMs within an artificial spin ice lattice is a relatively simple means to move beyond planar structures in the field of reconfigurable MCs and microwave filter applications that is compatible with industrial patterning processes.

Data availability statement

The data that support the findings of this study are available upon reasonable request from the authors.

Acknowledgments

Dr Navab Singh is thanked for the DUV templates. The authors thank Dr David Lloyd and Prof. Atsufumi Hirohata for assistance during VSM measurements performed at the University of York. Additional VSM-PPMS measurements were performed at Oklahoma State University and was supported by the NSF MRI Program through Grant No. 2216233. SEM imaging of the patterned structures were carried out in the Microscopy Laboratory, Oklahoma State University, which received funds for purchasing the equipment from the NSF MRI program. Micromagnetic simulations were completed utilizing the High Performance Computing Center facilities of Oklahoma State University at Stillwater. XMaS is a UK national research facility supported by EPSRC. We are grateful to Laurence Bouchenoire for their support and thanks to Tom Hase at Warwick and Debi Rianto at Durham for analysis of the in-plane x-ray scattering data. AOA would like to thank the Royal Society Wolfson Fellowship.

ORCID iDs

Julius de Rojas https://orcid.org/0000-0002-1206-4744
Del Atkinson https://orcid.org/0000-0002-9438-7407
Adekunle O Adeyeye https://orcid.org/0000-0001-9724-2468

References

[1] Markov I L 2014 *Nature* **512** 147
[2] Esmaeilzadeh H, Blem E, Amant R S, Sankaralingam K and Burger D 2011 *2011 38th Annual Int. Symp. on Computer Architecture (ISCA) (2011 38th Annual Int. Symp. on Computer Architecture (ISCA))* pp 365–76
[3] Barman A, Mondal S, Sahoo S and De A 2020 *J. Appl. Phys.* **128** 170901
[4] Sadovnikov A V, Gubanov V A, Sheshukova S E, Sharaevskii Y and Nikitov S A 2018 *Phys. Rev. Appl.* **9** 051002
[5] Chumak A V, Serga A A and Hillebrands B 2017 *J. Phys. D: Appl. Phys.* **50** 244001
[6] Barman A *et al* 2021 *J. Phys.: Condens. Matter* **33** 413001
[7] Chumak A V, Vasyuchka V I, Serga A A and Hillebrands B 2015 *Nat. Phys.* **11** 453
[8] Hirohata A, Yamada K, Nakatani Y, Prejbeanu I-L, Diény B, Pirro P and Hillebrands B 2020 *J. Magn. Magn. Mater.* **509** 166711
[9] Neusser S and Grundler D 2009 *Adv. Mater.* **21** 2927
[10] Grundler D 2015 *Nat. Phys.* **11** 438
[11] Chumak A V, Serga A A and Hillebrands B 2014 *Nat. Commun.* **5** 4700
[12] Wang Q, Hamadeh A, Verba R, Lomakin V, Mohseni M, Hillebrands B, Chumak A V and Pirro P 2020 *npj Comput. Mater.* **6** 192
[13] Wang Q, Chumak A V and Pirro P 2021 *Nat. Commun.* **12** 2636
[14] Papp A, Porod W and Csaba G 2021 *Nat. Commun.* **12** 6422
[15] Fukami S and Ohno H 2018 *J. Appl. Phys.* **124** 151904
[16] Brächer T and Pirro P 2018 *J. Appl. Phys.* **124** 152119
[17] Gartside J C, Stenning K D, Vanstone A, Holder H H, Arroo D M, Dion T, Caravelli F, Kurebayashi H and Branford W R 2022 *Nat. Nanotechnol.* **17** 460
[18] Allwood D A *et al* 2023 *Appl. Phys. Lett.* **122** 040501
[19] Fischer T, Kewenig M, Bozhko D A, Serga A A, Syvorotka I I, Ciubotaru F, Adelmann C, Hillebrands B and Chumak A V 2017 *Appl. Phys. Lett.* **110** 152401
[20] Kostylev M P, Serga A A, Schneider T, Leven B and Hillebrands B 2005 *Appl. Phys. Lett.* **87** 153501
[21] Khitun A and Wang K L 2011 *J. Appl. Phys.* **110** 034306
[22] Demokritov S O and Hillebrands B 2002 Spinwaves in laterally confined magnetic structures *Spin Dynamics in Confined Magnetic Structures I* ed B Hillebrands and K Ounadjela (Springer) pp 65–92
[23] Di K, Feng S X, Piramanayagam S N, Zhang V L, Lim H S, Ng S C and Kuok M H 2015 *Sci. Rep.* **5** 10153
[24] Gubbiotti G, Zhou X, Adeyeye A O, Varvaro G and Kostylev M 2020 *Phys. Rev.* B **101** 224431
[25] Kuchibhotla M, Haldar A and Adeyeye A O 2024 *J. Appl. Phys.* **135** 103903
[26] Tang W, Zhou Z-W, Nie Y-Z, Xia Q-L, Zeng Z-M and Guo G-H 2017 *Appl. Phys. Lett.* **111** 172407
[27] De A, Mondal S, Banerjee C, Chaurasiya A K, Mandal R, Otani Y, Mitra R K and Barman A 2017 *J. Phys. D: Appl. Phys.* **50** 385002
[28] Mandal R, Saha S, Kumar D, Barman S, Pal S, Das K, Raychaudhuri A K, Fukuma Y, Otani Y and Barman A 2012 *ACS Nano* **6** 3397
[29] Kumar D, Sabareesan P, Wang W, Fangohr H and Barman A 2013 *J. Appl. Phys.* **114** 023910
[30] Choudhury S, Barman S, Otani Y and Barman A 2017 *ACS Nano* **11** 8814
[31] Mallick S, Mishra S S and Bedanta S 2018 *Sci. Rep.* **8** 11648
[32] Kuchibhotla M, Talapatra A, Haldar A and Adeyeye A O 2021 *J. Appl. Phys.* **130** 083906
[33] Tian C and Adeyeye A O 2024 *Nanoscale* **16** 4858
[34] Kaffash M T, Lendinez S and Jungfleisch M B 2021 *Phys. Lett.* A **402** 127364
[35] Chumak A V *et al* 2022 *IEEE Trans. Magn.* **58** 1
[36] Skjærvø S H, Marrows C H, Stamps R L and Heyderman L J 2020 *Nat. Rev. Phys.* **2** 13
[37] Gliga S, Iacocca E and Heinonen O G 2020 *APL Mater.* **8** 040911
[38] Anghinolfi L, Luetkens H, Perron J, Flokstra M G, Sendetskyi O, Suter A, Prokscha T, Derlet P M, Lee S L and Heyderman L J 2015 *Nat. Commun.* **6** 8278
[39] Canals B, Chioar I-A, Nguyen V-D, Hehn M, Lacour D, Montaigne F, Locatelli A, Menteş T O, Burgos B S and Rougemaille N 2016 *Nat. Commun.* **7** 11446
[40] Nisoli C, Kapaklis V and Schiffer P 2017 *Nat. Phys.* **13** 200
[41] Schiffer P and Nisoli C 2021 *Appl. Phys. Lett.* **118** 110501
[42] Wyss M, Gliga S, Vasyukov D, Ceccarelli L, Romagnoli G, Cui J, Kleibert A, Stamps R L and Poggio M 2019 *ACS Nano* **13** 13910
[43] Gliga S, Kákay A, Hertel R and Heinonen O G 2013 *Phys. Rev. Lett.* **110** 117205
[44] Ghosh A, Ma F, Lourembam J, Jin X, Maddu R, Yap Q J and Ter Lim S 2020 *Nano Lett.* **20** 109
[45] Bhat V S, Watanabe S, Baumgaertl K, Kleibert A, Schoen M A W, Vaz C A F and Grundler D 2020 *Phys. Rev. Lett.* **125** 117208
[46] Lendinez S and Jungfleisch M B 2019 *J. Phys.: Condens. Matter* **32** 013001
[47] Iacocca E, Gliga S, Stamps R L and Heinonen O 2016 *Phys. Rev.* B **93** 134420
[48] Iacocca E and Heinonen O 2017 *Phys. Rev. Appl.* **8** 034015
[49] Iacocca E, Gliga S and Heinonen O G 2020 *Phys. Rev. Appl.* **13** 044047
[50] Talapatra A, Singh N and Adeyeye A O 2020 *Phys. Rev. Appl.* **13** 014034
[51] Gartside J C, Vanstone A, Dion T, Stenning K D, Arroo D M, Kurebayashi H and Branford W R 2021 *Nat. Commun.* **12** 2488
[52] Ladak S, Read D E, Perkins G K, Cohen L F and Branford W R 2010 *Nat. Phys.* **6** 359
[53] Bang W, Sturm J, Silvani R, Kaffash M T, Hoffmann A, Ketterson J B, Montoncello F and Jungfleisch M B 2020 *Phys. Rev. Appl.* **14** 014079
[54] Dion T, Arroo D M, Yamanoi K, Kimura T, Gartside J C, Cohen L F, Kurebayashi H and Branford W R 2019 *Phys. Rev.* B **100** 054433
[55] Gilbert I, Lao Y, Carrasquillo I, O'Brien L, Watts J D, Manno M, Leighton C, Scholl A, Nisoli C and Schiffer P 2016 *Nat. Phys.* **12** 162
[56] Macêdo R, Macauley G M, Nascimento F S and Stamps R L 2018 *Phys. Rev.* B **98** 014437
[57] Lao Y *et al* 2018 *Nat. Phys.* **14** 723
[58] Saha S, Zhou J, Hofhuis K, Kákay A, Scagnoli V, Heyderman L J and Gliga S 2021 *Nano Lett.* **21** 2382
[59] Sklenar J, Lao Y, Albrecht A, Watts J D, Nisoli C, Chern G-W and Schiffer P 2019 *Nat. Phys.* **15** 191
[60] Ladak S, Fernández-Pacheco A and Fischer P 2022 *APL Mater.* **10** 120401
[61] Fernández-Pacheco A, Streubel R, Fruchart O, Hertel R, Fischer P and Cowburn R P 2017 *Nat. Commun.* **8** 15756
[62] Sahoo S, May A, van Den Berg A, Mondal A K, Ladak S and Barman A 2021 *Nano Lett.* **21** 4629
[63] Sahoo S, Mondal S, Williams G, May A, Ladak S and Barman A 2018 *Nanoscale* **10** 9981
[64] May A, Hunt M, Van Den Berg A, Hejazi A and Ladak S 2019 *Commun. Phys.* **2** 13
[65] May A, Saccone M, van den Berg A, Askey J, Hunt M and Ladak S 2021 *Nat. Commun.* **12** 3217

[66] Llandro J *et al* 2020 *Nano Lett.* **20** 3642
[67] Dobrovolskiy O V *et al* 2021 *Appl. Phys. Lett.* **118** 132405
[68] Saccone M, Scholl A, Velten S, Dhuey S, Hofhuis K, Wuth C, Huang Y-L, Chen Z, Chopdekar R V and Farhan A 2019 *Phys. Rev.* B **99** 224403
[69] Saccone M, Van den Berg A, Harding E, Singh S, Giblin S R, Flicker F and Ladak S 2023 *Commun. Phys.* **6** 217
[70] Saccone M, Caravelli F, Hofhuis K, Parchenko S, Birkhölzer Y A, Dhuey S, Kleibert A, van Dijken S, Nisoli C and Farhan A 2022 *Nat. Phys.* **18** 517
[71] Skoric L *et al* 2022 *ACS Nano* **16** 8860
[72] Donnelly C *et al* 2015 *Phys. Rev. Lett.* **114** 115501
[73] Pip P *et al* 2022 *APL Mater.* **10** 101101
[74] de Rojas J, Atkinson D and Adeyeye A O 2023 *Appl. Phys. Lett.* **123** 232407
[75] Dion T *et al* 2024 *Nat. Commun.* **15** 4077
[76] Adeyeye A O and Singh N 2008 *J. Phys. D: Appl. Phys.* **41** 153001
[77] Vansteenkiste A, Leliaert J, Dvornik M, Helsen M, Garcia-Sanchez F and Van Waeyenberge B 2014 *AIP Adv.* **4** 107133
[78] Najafi M *et al* 2009 *J. Appl. Phys.* **105** 113914
[79] Kittel C 1948 *Phys. Rev.* **73** 155
[80] Cronemeyer D C 1991 *J. Appl. Phys.* **70** 2911
[81] Haldar A, Kumar D and Adeyeye A O 2016 *Nat. Nanotechnol.* **11** 437